

Comprehensive Real-Time Hardware-In-the-Loop Transient Emulation of MVDC Power Distribution System on Nuclear Submarine

WEIRAN CHEN  (Student Member, IEEE), TIAN LIANG  (Member, IEEE),
AND VENKATA DINAHAHI  (Fellow, IEEE)

Department of Electrical and Computer Engineering, University of Alberta, Edmonton, Alberta T6G 2V4, Canada

CORRESPONDING AUTHOR: TIAN LIANG (e-mail: tian.liang@ualberta.ca).

This work was supported by the Natural Science and Engineering Research Council of Canada (NSERC).

ABSTRACT A nuclear submarine has significant performance advantages over the conventional diesel-electric submarine. Its powerful nuclear propulsion can be operated independently of air and does not require refueling throughout the 25-year life span. Recent progresses of medium voltage direct current (MVDC) techniques applied in industry push the energy-saving and extremely long-time operation to a new stage with a feasible solution of smaller scale nuclear reactor embedded inside the vessel. Thus, there is a need to investigate the new MVDC-based nuclear submarine power distribution system and its real-time hardware-in-the-loop (HIL) emulation to test the control systems, device stresses, etc. This paper proposes a comprehensive MVDC-based nuclear submarine power distribution system emulated in real-time on a multi-FPGA hardware platform with system-level transients (validated by Matlab/Simulink) at 20 μ s time-step and device-level transients (validated by SaberRD) at 400 ns time-step.

INDEX TERMS Electromagnetic transients, field-programmable gate arrays (FPGAs), hardware-in-the-loop (HIL) emulation, marine propulsion, medium voltage direct current (MVDC), nuclear submarine, pressurized water reactor, real-time systems.

I. INTRODUCTION

A submarine is a vital strategic asset of marine forces designated primarily for naval and amphibious warfare. Admittedly, it provides intelligence services and marine protection for surface ships, amphibious ships, and seaborne aviation. However, conventional diesel-electric submarine lost its position when the first nuclear-powered submarine USS Nautilus was commissioned back in 1958 [1]. Unquestionably, nuclear-powered submarine propulsion system allows the vessel for longer operation time beneath the deep water, higher stealthiness during warfare, and less on-duty refueling demand. With multiple advantages mentioned above, the US Navy projected \$69 billion more than the original plan of congressional budget office for the next decades on new strategic submarine technology [2].

Presently, the nuclear-powered propulsion system still adopts the traditional medium voltage alternating current (MVAC) power distribution system. With the recent progresses of medium voltage direct current (MVDC) techniques applied in industry, MVDC-based distribution for next generation ships and marine vessels is drawing tremendous attention from engineers and scientists for improving the energy-efficiency [3], [4], testing the device and components operation stresses [5], redesigning the vessel mechanical structures and electrical topologies [6]–[9], etc.

For early stages of design and evaluation of the MVDC-based nuclear submarine power distribution system, it is necessary to utilize hardware-in-the-loop (HIL) techniques for power electronic device selection, electrical topology redesign, device-level and system-level performance

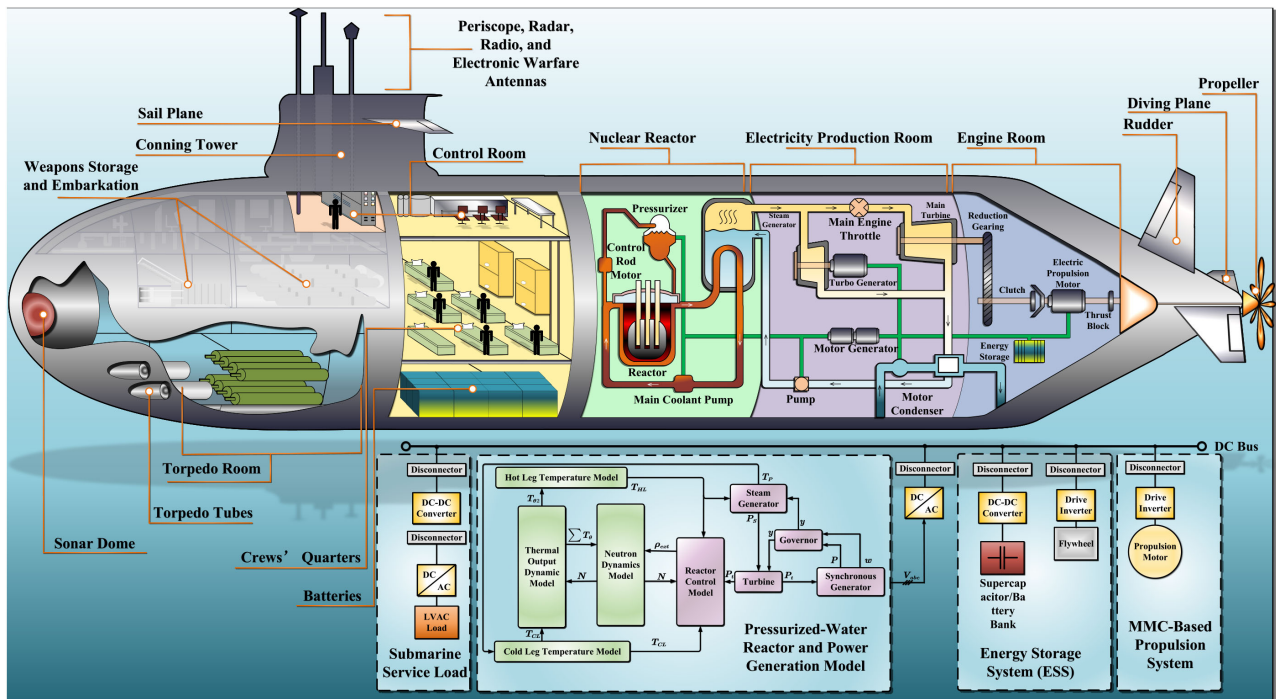


FIGURE 1. Overview of nuclear submarine MVDC power distribution system.

assessment, system control optimization, etc., to reduce the development cycle and capital investment. Simulating the comprehensive MVDC-based nuclear submarine power distribution system in real-time is challenging for traditional general-purpose compute unit, such as micro-controller, central processing unit (CPU), etc. In this scenario, paralleled compute structure, such as graphics processing unit (GPU) and field-programmable gate array (FPGA), are advantageous over the sequential general purpose for the inherent hierarchical paralleled MVDC power distribution system [10]. However, GPU suffers from the communication time latency between simulator processors (about one microsecond), which makes its real-time capability unfeasible for the emulation. Differently, FPGA can conduct the real-time emulation in parallel with optimized block-to-block communication width and speed, which has been proven in the area of transportation electrification [11], renewable energy [12], power transmission and distribution [13], power electronic devices [14]–[16], etc.

Some efforts in the literature were devoted to the real-time simulation of MVDC marine power system and nuclear reactor such as [17]–[21]; however, these works either use merely a notional model or focus on only a small part of the system. So far there is no publication in the literature that shows how to cope with the simulation of operation of the overall MVDC power system on nuclear submarine, neither in off-line nor real-time conditions. This paper fills this gap by developing a comprehensive real-time hardware-in-the-loop emulation of MVDC-based power distribution system of nuclear submarine with all the major components at both system-level

and device-level on a multi-FPGA hardware platform. The structure of the rest sections in this paper is organized as follows: Section II discusses the nuclear generation, modular multilevel converter (MMC) based motor propulsion system, energy storage system, and submarine service load. The hardware design of the real-time submarine power distribution system on multiple FPGAs is illustrated in Section III. Section IV presents the results and comparisons. Finally, the conclusion and future work are demonstrated in Section V.

II. MVDC-BASED NUCLEAR SUBMARINE POWER DISTRIBUTION SYSTEM

In this section, reconfigurable modular subsystems, including nuclear generation, MMC-based motor propulsion system, energy storage system, and the submarine service load are introduced in detail. All mathematical models have been discretized by Trapezoidal rule and given by corresponding formulas or references. The comprehensive nuclear submarine power distribution system diagram is shown in Fig. 1.

A. NUCLEAR GENERATION

The pressurized-water reactor (PWR) makes up the majority of the proportion of usage in nuclear-powered submarines, for example, the Ohio-class and Los Angeles-class nuclear submarines from the US Navy [22]. In the 1950s, PWRs were initially developed in the US for nuclear submarine power plants [23]. After research and development for nearly half a century, around 490 nuclear submarines and 700 nuclear power plants have been built all over the world, of which 98.4% are PWRs. By 2019, based on published literature,

there are approximately 140 active nuclear submarines, including 70 in the US, around 40 in Russia, 19 in China, 10 in the UK, 9 in France, and 3 in India [24]. A typical nuclear submarine PWR is composed of two main circuits: 1) nuclear reactor, pressurizer, coolant pump, and control rod; 2) steam generator, turbo-generator set, and accessory equipment.

In order to study the dynamic responses of the power distribution system interconnect between PWR and submarine, it is important to choose an appropriate mathematical model. In recent years, a lot of research established the PWR mathematical model [25]–[27] including a detailed PWR linearized mathematical model expressed by 55-order differential equations. In this work, a 21-order differential equation lumped parameter model of PWR is used for power distribution system transient studies purposes, presented mainly in [28]–[31]. This model consists of kinetics model of the reactor, thermal output dynamic system, hot-leg and cold-leg temperature model, steam generation model, reactor control system model, and turbo-generator set model, as shown in the Fig. 1.

1) POINT KINETICS MODEL OF THE REACTOR

The reactor dynamic model mainly shows the neutron dynamic behaviour in the nuclear reactor, where the changes of neutron density correspond to the modification of the reactor thermal power. Reference [28] indicates that the reactor power is proportional to the neutron flux and the average neutron density, as expressed below:

$$P_{th}(t) \sim \varnothing \sim \tilde{n}, \quad (1)$$

$$P_{th}(t) = \frac{\tilde{n}}{N_{0,N}} P_{th,N}, \quad (2)$$

where \tilde{n} is the mean neutron density; $N_{0,N}$ is the nominal average neutron density; P_{th} is the reactor thermal power; $P_{th,N}$ is the nominal power of the reactor; and \varnothing is the neutron flux. For the calculation simplicity, (2) is normalized and linearized using the incremental method. Besides, it is assumed that the changes of time and position in the reactor do not affect neutron density; only the effect of temperature feedback on reactivity and six groups of delayed neutrons are taken into consideration. Equations are revealed as below:

$$\frac{d\Delta n(t)}{dt} = \frac{\Delta\rho(t)}{l} - \frac{\beta}{l} d\Delta n(t) + \sum_{\lambda=1}^6 \lambda_i \Delta C_i(t), \quad (3)$$

$$\frac{d\Delta C_i(t)}{dt} = \frac{\beta_i}{l} d\Delta n(t) - \sum_{\lambda=1}^6 \lambda_i \Delta C_i(t), \quad (4)$$

$$\Delta\rho(t) = \beta \Delta\rho_{ext} + \alpha_F \Delta T_F + \alpha_C \left(\frac{\Delta T_{\theta 1} + \Delta T_{\theta 2}}{2} \right), \quad (5)$$

where $\Delta n(t)$ is the neutron flux deviation; $\Delta\rho$ is the reactivity deviation; $\Delta\rho_{ext}$ is the reactivity change induced by control rod; ΔT_F is the fuel temperature deviation; $\Delta T_{\theta 1}$ and $\Delta T_{\theta 2}$ are the temperature deviation in coolant node 1 and 2, respectively; l is the neutron generation time; β is the delayed neutron group fraction; β_i is the delayed neutron fraction of the i th group; λ_i is the equivalent decay constant; α_F is the

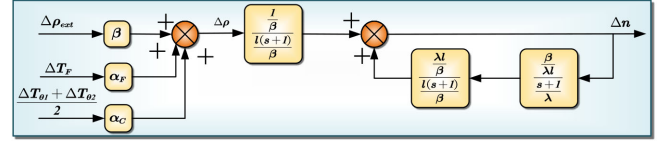


FIGURE 2. Reactor neutron dynamics model.

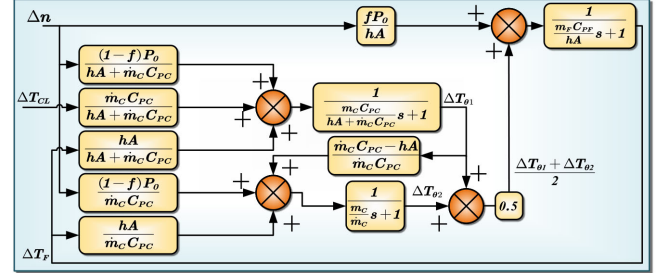


FIGURE 3. Thermal output dynamic model.

fuel coefficient of reactivity; and α_C is the coolant coefficient of reactivity. The transfer block diagram is illustrated in Fig. 2.

2) THERMAL OUTPUT DYNAMIC MODEL

The energy generated by nuclear fission leads to the rise of fuel temperature, and then the heat is transferred to the coolant. The model consists of one fuel node and two coolant nodes. From the energy balance equation, the thermal output dynamic model is derived as below:

$$\frac{d\Delta T_F}{dt} = \frac{fP_0}{m_F C_{PF}} \Delta n + \frac{hA}{2m_F C_{PF}} (\Delta T_{\theta 1} + \Delta T_{\theta 2} - 2\Delta T_F), \quad (6)$$

$$\frac{d\Delta T_{\theta 1}}{dt} = \frac{(1-f)P_0}{m_C C_{PC}} \Delta n + \frac{hA}{m_C C_{PC}} (\Delta T_F - \Delta T_{\theta 1}) + \frac{\dot{m}_C}{m_C} (\Delta T_{CL} - \Delta T_{\theta 1}), \quad (7)$$

$$\frac{d\Delta T_{\theta 2}}{dt} = \frac{(1-f)P_0}{m_C C_{PC}} \Delta n + \frac{hA}{m_C C_{PC}} (\Delta T_F - \Delta T_{\theta 1}) + \frac{\dot{m}_C}{m_C} (\Delta T_{\theta 1} - \Delta T_{\theta 2}), \quad (8)$$

where P_0 is the initial power of reactor; f is the fraction of the total power produced in the fuel; h is the heat transfer coefficient from fuel to coolant; A is the heat transfer area; m_F is the mass of fuel; C_{PF} is the specific heat of fuel; m_C is the mass of coolant; C_{PC} is the specific heat of coolant; and \dot{m}_C is the mass flow rate in core. The transfer function block diagram is illustrated in Fig. 3.

3) HOT-LEG AND COLD-LEG TEMPERATURE MODEL

A first-order inertial model is used to represent the reactor coolant in/outlet cavity, the steam generator's coolant out/inlet cavity, and the coolant pipe. Therefore, these three parts can be combined collectively and referred to as hot-leg and cold-leg. The transfer function block diagram is shown as Fig. 4,

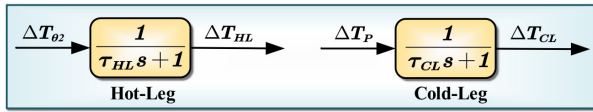


FIGURE 4. Hot-leg and cold-leg temperature model.

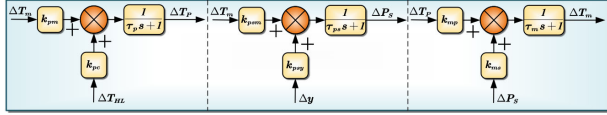


FIGURE 5. Steam generator model.

where ΔT_{HL} is the hot-leg temperature deviation; ΔT_{CL} is the cold-leg temperature deviation; ΔT_P is the primary fluid lump temperature deviation; τ_{HL} is the hot-leg heat transfer time constant; and τ_{CL} is the cold-leg heat transfer time constant.

4) STEAM GENERATOR MODEL

The U-tube steam generator (UTSG) is the bridge of the heat transfer from primary circuit to secondary circuit. The steam generator consists of three parts: the average temperature module of primary coolant, the heat transfer module of U-shape tube, and the steam pressure module of secondary circuit. The lumped parameter mathematical model is listed as follows:

$$\frac{d\Delta T_P}{dt} = \frac{1}{\tau_P} (k_{pm}\Delta T_m + k_{pc}\Delta T_{HL} - \Delta T_P), \quad (9)$$

$$\frac{d\Delta T_m}{dt} = \frac{1}{\tau_m} (k_{mp}\Delta T_P + k_{ms}\Delta P_S - \Delta T_m), \quad (10)$$

$$\frac{d\Delta P_S}{dt} = \frac{1}{\tau_{PS}} (k_{psm}\Delta T_m + k_{psv}\Delta y - \Delta P_S), \quad (11)$$

where ΔT_m is the tube metal lump temperature deviation; ΔP_S is the steam pressure deviation; τ_P , τ_m , and τ_{PS} are the coolant, U-type metal tube, and steam pressure time constants, respectively; Δy is the fractional change in valve coefficient; and k_{pm} , k_{mp} , k_{pc} , k_{ms} , k_{psm} , and k_{psv} are metal tube temperature, coolant temperature, hot leg temperature, pressure temperature, metal tube pressure, and valve pressure coefficient, respectively. The transfer function block diagram can be observed in Fig. 5.

5) REACTOR CONTROL SYSTEM MODEL

In the PWR, the reactor control system model regulates the reactivity by changing the position of the control rod, and also regulates the steam pressure of the secondary circuit through the pressurizer, so as to start, stop or change the reactor output power. Generally, there are two basic control approaches: 1) coolant average temperature control mode, which mainly focuses on the constant primary coolant temperature but increases the burden of the secondary circuit; 2) the constant steam pressure control mode, which keeps steam pressure of the secondary circuit unchanged, but makes the burden of the

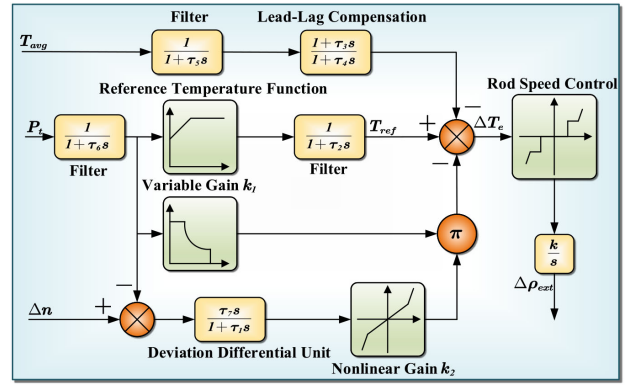


FIGURE 6. Reactor control model.

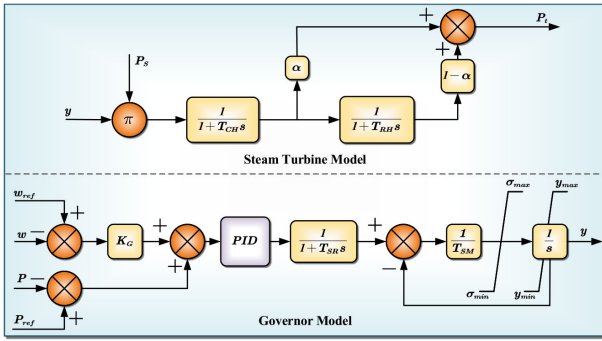
primary circuit heavier [30], [32]. In this work, the first control mode is utilized.

The coolant average temperature control system is mainly composed of three nonlinear regulation channels: 1) average temperature measurement channel; 2) average reference temperature setting channel; and 3) power mismatch channel [32]. In the first channel, T_{avg} is the arithmetic mean of T_{CL} and T_{HL} . Besides, the lead-lag compensation is used to compensate the lag response of the measurement channel caused by thermal inertia. The function of filter is to eliminate the thermal noise of temperature sensors. In the second channel, the reference average temperature is determined by the turbine output power and steady-state operation plan. Then the filter eliminates slight and sharp disturbance signals to avoid frequent actions of the control rods. In the third channel, since the whole PWR system has a large inertia link and a long transition time of temperature change, the power mismatch control is used to accelerate the response speed of the system. In case of sudden load change or disturbance, the power deviation generates differential signals through the deviation differential unit, which is calibrated by nonlinear gain and variable gain before entering the adder to participate in the control. Due to the effect of the deviation differential unit, the response signals depend on the changing speed deviation. Finally, according to the output value of the adder, the rod speed signal will be output through the control rod logic device. In this model, the change of reactor reactivity is the final output. The control model is shown as Fig. 6, where $T_{avg} = \frac{T_{CL} + T_{HL}}{2}$; T_{ref} is the reference temperature; ΔT_e is the temperature deviation; P_t is the turbine output power; $\tau_{1\sim 7}$ is the time constant; k_1 is the variable gain; and k_2 is the nonlinear gain. The Laplace transformation of temperature deviation is given as follows:

$$\Delta T_e = \frac{T_{ref}}{1 + \tau_2 s} - \frac{1 + \tau_3 s}{(1 + \tau_4 s)(1 + \tau_5 s)} T_{avg} - \frac{k_1 k_2 \tau_7 s}{1 + \tau_1 s} \left(\Delta n - \frac{P_t}{1 + \tau_6 s} \right). \quad (12)$$

6) TURBO-SET AND GENERATOR

In this work, a simplified turbo-set model is adopted, which only considers the volume effect of high pressure steam and

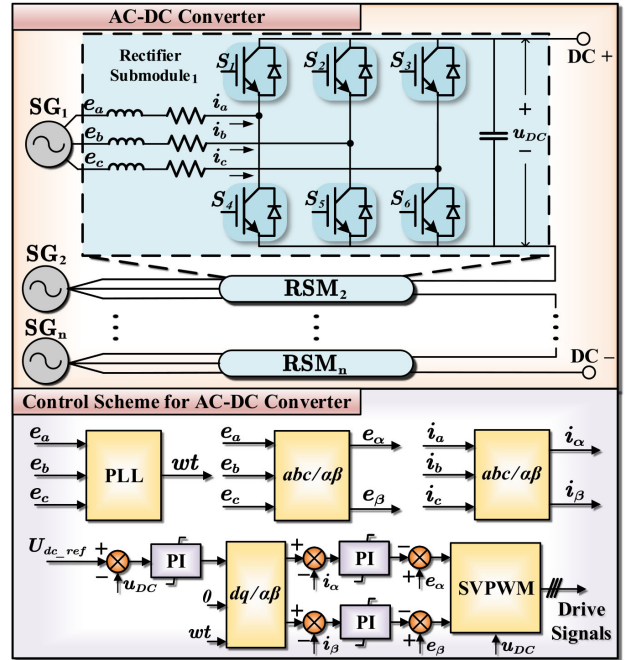
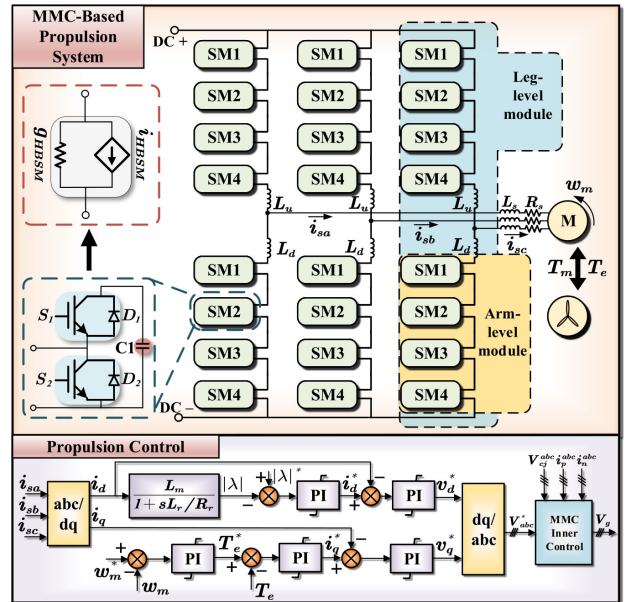

FIGURE 7. Turbo-set and governor models.

reheat steam. The governor model is of the common power frequency electro-hydraulic type. Both are shown in Fig. 7, where y is the steam turbine value; P_t is the turbine output power; P is the output power of synchronous motor; P_{ref} is the reference power; w is the motor speed; w_{ref} is the reference motor speed; P_s is the steam pressure; T_{CH} is the turbine volume time constant; T_{RH} is the reheat time constant; α is the steam proportion coefficient of high-pressure cylinder; K_G is the governor gain; T_{SR} is the time constant of the relay; T_{SM} is the servomotor integral time constant; σ_{max} and σ_{min} are the valve opening speed limits; and y_{max} and y_{min} limit the range of the valve.

A 20 MW, 13.8 kV, 1800 rpm synchronous generator is used. In this work, the synchronous machine model follows the IEEE Std. 1110-2002 [33]. The electrical part of the machine is represented by a sixth-order state-space model and the mechanical part is approximated by a second-order function. Being installed in a DC system, there is an advantage that the output voltage of the synchronous generator does not have to operate at a fixed frequency, which means variable speed can be achieved to save fuel. The AC/DC converter, or rectifier, is used to convert the voltage from AC into DC to feed the main DC bus. The active rectifier can reduce the low input current harmonics, smooth output voltage, and regulate its output voltage variation. Also, different power-sharing algorithms can be realized. Among the various active rectifiers, the three-phase SVPWM rectifier with the double closed-loop control strategy is employed in this simulation system. Considering that the voltage on the DC bus is relatively high, the DC output voltage of converter can be configured in a series cascaded configuration with several identical submodules. The overall illustration of the generation system and control scheme is given in Fig. 8, where $e_{a,b,c}$ and $i_{a,b,c}$ are input voltages and currents for individual rectifier circuit, and u_{DC} is the output DC voltage.

B. MMC-BASED MOTOR PROPULSION SYSTEM

The overall structure of the MMC-based motor propulsion system is shown in Fig. 9, where a five-level MMC topology is chosen. Each submodule consists of two IGBT switches and one capacitor, seen as a half-bridge. The MMC-based motor is connected to the DC bus in parallel and drives the submarine.


FIGURE 8. Synchronous generators and converter control scheme.

FIGURE 9. MMC-based motor propulsion system.

The control strategy is also illustrated in Fig. 9, which involves two parts: one is the phase-shifted carrier-based PWM (PSC-PWM) control inside MMC [34], [38]–[40]; and the other is the current/speed double closed-loop control of the motor [35]–[37]. In Fig. 9, i_{sa} , i_{sb} , and i_{sc} are three-phase stator currents; V_{cj}^{abc} is the j th three-phase submodule capacitor voltage; i_p^{abc} and i_n^{abc} are the three-phase MMC upper and lower arm current, respectively; w_m , T_e , and λ are the motor speed, electromagnetic torques, and flux, respectively; and w_m^* , T_e^* , and λ^* are their reference values, respectively.

All the parameters above are used as the input signals of the controller, which produces modulation signals V_{abc}^* as inputs of the MMC inner controller. After that, the MMC converter generates driving pulses V_g as the control signals of switches.

In terms of the modeling of MMC submodule, the half-bridge is converted into an equivalent combination of conductance and voltage-controlled current source (VCCS). Every component of the submodule can be seen as a conductance paralleled with a controlled current source in the Norton equivalent, as shown in Fig. 9, wherein g_{HBSM} and i_{HBSM} are the equivalent conductance and VCCS of the half-bridge submodule, respectively [41].

The modeling of asynchronous machine used for propulsion is based on the combination of an electrical part and a mechanical part, represented by a fourth-order and second-order state-space models, respectively [42], and the motor speed is assumed to be the propeller speed.

Besides, it is important to choose an appropriate load for the submarine propulsion system. Generally, when the submarine moves in water, it will be affected by the pressure perpendicular to the hull surface, mainly caused by wave-making resistance. Meanwhile, it will also be affected by the tangential force of water flow along the surface, namely the friction resistance. Furthermore, there are many additional resistances to consider, mainly including the fouling resistance caused by paint peeling off, corrosion, and adhesion of aquatic organisms, the rough-sea resistance caused by wind and waves, the appendage resistance caused by appendages such as control tower and rudder, the form drag caused by the submarine shape and flow holes, etc. For more detailed modeling, such as propeller modeling, the effects of wake current and thrust deduction should also be considered [43]. According to previous theoretical analysis and experimental results, when the submarine is sailing at a depth of more than one-third of its length from the water surface, the wave-making resistance is negligible, and the friction resistance accounts for about 80% of the total resistance. Therefore, in this work, only the friction resistance R_F is considered, expressed by the following formula:

$$R_F = \frac{1}{2} \rho_{sw} v_{sm}^2 S K_F, \quad (13)$$

where ρ_{sw} is the seawater density; v_{sm} represents the speed of the submarine; S is the wetted area; and K_F is friction coefficient.

C. ENERGY STORAGE SYSTEM

The energy storage system is another crucial part of microgrid to mitigate the contradiction of power and demand, especially when a single load (like the propulsion system) consumes the majority of the power. The typical forms of energy storage type include battery, supercapacitor, fly-wheel, etc. In this emulation, considering the high energy density required to support the DC bus and the complex requirements in practical application, all three cases are modeled.

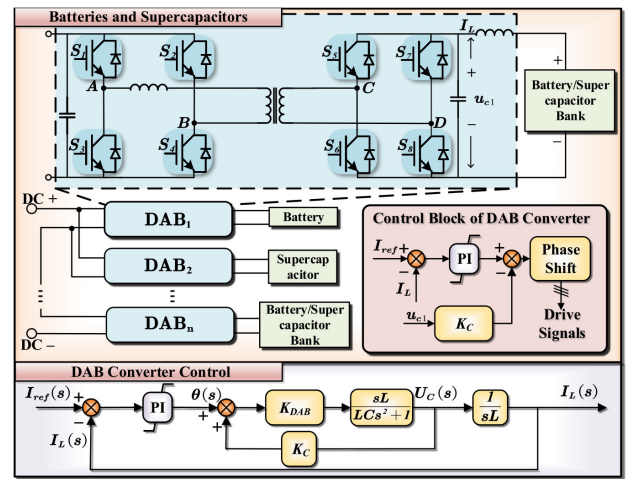


FIGURE 10. Configuration of batteries and supercapacitors in energy storage system.

1) BATTERIES AND SUPERCAPACITORS

The dual active bridge (DAB) converter is chosen as the fundamental element to build the power exchange converter. The overall system is illustrated in Fig. 10. Several DAB converters are connected in series on the primary side to interface with the main DC bus. The secondary side is connected with batteries and supercapacitors, which are in parallel through the DAB. Generally, all the submodules work identically; however, working asymmetrically is allowed as long as the primary side voltage does not exceed the hazardous region. The control block of the DAB converter is also depicted in Fig. 10. There is only one control variable, namely the phase difference between the primary and secondary sides of the bridge, in this system. Power always goes from the leading phase side to the lagging side. A PI controller is used to control the power flow between the DC bus and the battery/supercapacitor bank. However, resonance can be triggered easily because there is an inductance and capacitance connected in parallel. So the capacitance-voltage is used as state feedback to suppress the resonance. The transfer function can be derived as follows:

$$\frac{\theta(s)}{I_L(s)} = \frac{K_{DAB}}{LCs^2 + K_{DAB}K_C Ls + 1}. \quad (14)$$

A first-order term appears in the denominator in (14), which can be viewed as the damping term. Thus active damping is achieved without any actual resistance to avoid losses.

The battery bank performs a generic dynamic model representing the most well-liked types of rechargeable batteries, which is a non-linear dynamic system combined with a controlled voltage source [44]. Besides, the supercapacitor proposed in this work is the Stern-Tafel model to describe the process of charge and discharge [45].

2) FLYWHEEL

The bi-directional power inverter and permanent magnet synchronous machine (PMSM) is adopted as the fundamental component, and the PMSM is connected directly with the

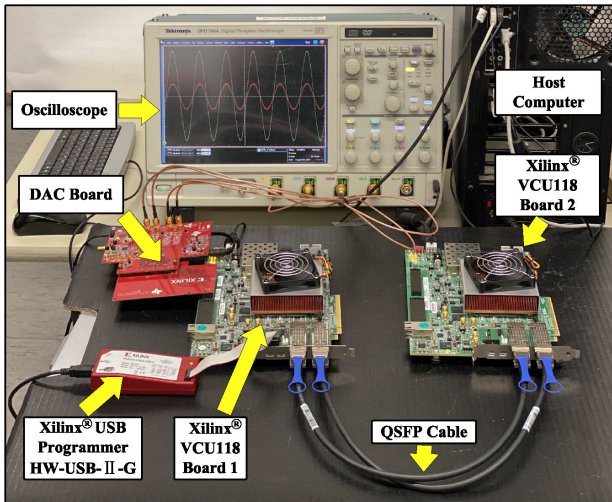


FIGURE 13. Hardware platform configuration used for MVDC-based nuclear submarine power distribution system emulation.

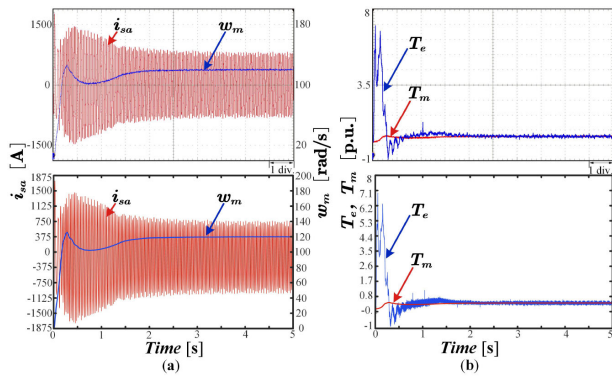


FIGURE 14. System-level results for propulsion system from real-time emulation (top) and Matlab/Simulink simulation (bottom). (a) Propeller speed w_m , and single-phase stator current i_{sa} . (b) Load torque T_m , and electromagnetic torque T_e . Scale: (a) (b) x-axis: 0.5 s/div.

(20 kV to 8 kV) power the thruster through device-level MMC inverter and the IGBT of ABB 5SNA 2000K450300 is utilized [47].

III. HARDWARE EMULATION OF NUCLEAR SUBMARINE POWER DISTRIBUTION SYSTEM

Considering the large system scale, in order to expand hardware resource capacity, the embedded MVDC-based nuclear submarine power distribution system was implemented on the two Xilinx Virtex UltraScale+ VCU118 FPGA boards which feature the XCVU9P FPGA with 1,182,240 look-up tables (LUTs), 2,364,480 flip-flops (FFs), 6,840 DSP slices, and 4,320 block RAMs (BRAMs) on each board. In terms of system-level subsystems, to balance hardware resource consumption and emulation latency, 100 MHz was selected as the operational frequency of FPGA board, with the corresponding clock period T_{clk} as 10 ns. For device-level subsystem, to perform appropriate time-step, 200 MHz corresponding to T_{clk} as 5 ns was chosen. With the help of Xilinx Vivado

TABLE 1. FPGA Hardware Resource Consumption of MVDC Power Subsystems on Nuclear Submarine

Module	Latency	BRAM	DSP	FF	LUT
System-Level MVDC Power System on VCU118-1 (100MHz)					
PWR-generation	1363 T_{clk}	3.935%	6.667%	1.875%	4.926%
Supercapacitor bank	1995 T_{clk}	2.570%	23.421%	9.992%	53.137%
Flywheel model	1619 T_{clk}	2.917%	3.626%	2.44%	5.884%
MMC propulsion system	970 T_{clk}	0.07%	16.89%	6.07%	21.08%
Total	-	9.422%	50.604%	20.377%	85.027%
System-Level MVDC Power System on VCU118-2 (200MHz)					
AC-DC converter	2572 T_{clk}	1.296%	23.284%	6.021%	12.810%
Submarine service load	1111 T_{clk}	1.319%	22.406%	5.382%	12.527%
Battery bank	1858 T_{clk}	1.111%	31.280%	10.858%	21.431%
Device-Level MVDC Power System on VCU118-2 (200MHz)					
MMC-based bow-thruster	80 T_{clk}	0%	20.760%	9.526%	21.316%
Total	-	3.726%	97.73%	31.787%	68.084%

high-level synthesis (HLS), the C code of MVDC-based nuclear submarine power distribution system was converted to VHDL code with optimized hardware resource allocation and reduced latency. After design synthesis and device mapping, the bitstreams were downloaded to the FPGA boards which transmitted the data from Xilinx FPGA Mezzanine Card (FMC) to digital-to-analog converters (DACs), and the oscilloscope presented the waveforms of real-time emulation results. Table 1 shows hardware design specifics, including the latency in clock cycles and the main hardware resource utilization. The two boards exchange data with each other by QSFP cable using Xilinx Aurora communication protocol, where the VCU118-1 FPGA board emulates the system-level nuclear generation, MMC propulsion system, supercapacitors bank, and flywheel model; while the VCU118-2 is used for the emulation of system-level AC-DC converter, submarine service load, and battery bank and device-level MMC-based bow-thruster. As listed in Table 1, the whole system was emulated at multiple rates and since the maximum latency of system-level submarine subsystems is 1995 T_{clk} , which is equivalent to 19.95 μ s, the output data was set to be updated per 20 μ s. The device-level MMC inverter model is included in submarine service load with 80 T_{clk} latency, which is equivalent to 400 ns. Fig. 13 shows the hardware platform configuration.

IV. HARDWARE EMULATION RESULTS AND VALIDATION OF NUCLEAR SUBMARINE POWER DISTRIBUTION SYSTEM

In this section, several typical operation mode results based on real-time hardware emulation of nuclear submarine power distribution system are presented, validated by off-line simulation tool Matlab/Simulink for system-level results and by SaberRD for device-level results. All the system parameters are provided in the Appendix and double precision (64bit) is chosen for all results. The average error is within 2%.

A. SUBMARINE DIVING MANEUVER

When performing periscope observation or receiving special signals, the submarine occasionally sails on or near the water

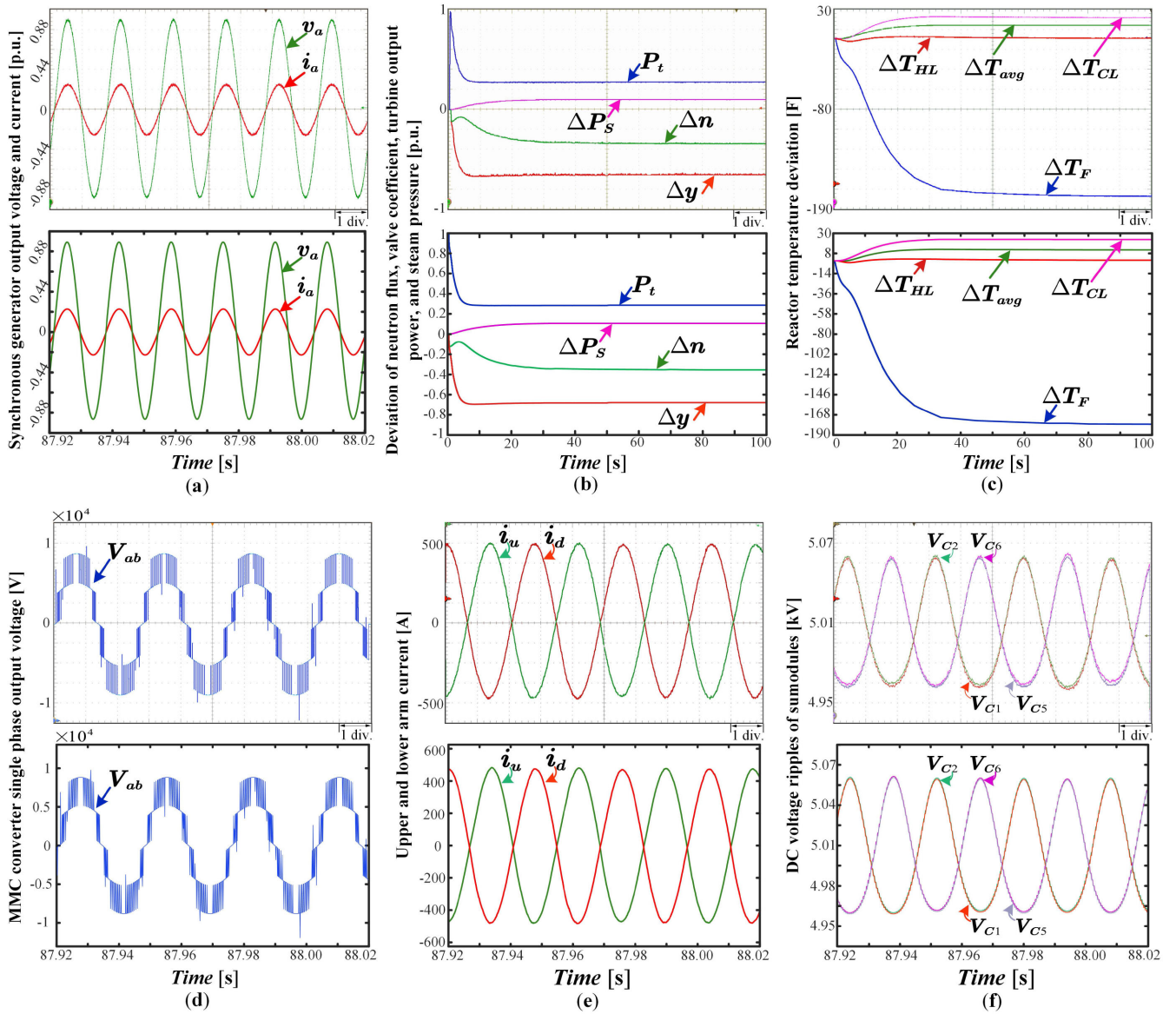


FIGURE 15. System-level results for MMC converter and nuclear reactor from real-time emulation (top) and Matlab/Simulink simulation (bottom). (a) Synchronous generator output voltage v_a and output current i_a . (b) Fractional change in valve coefficient Δy , turbine output power P_t , steam pressure deviation ΔP_s , neutron flux deviation Δn . (c) Hot-leg temperature deviation ΔT_{HL} , cold-leg temperature deviation ΔT_{CL} , coolant average temperature deviation ΔT_{avg} , and fuel temperature deviation ΔT_F . (d) MMC converter single phase output voltage V_{ab} . (e) Upper arm current i_u and lower arm current i_d . (f) DC voltage ripples of the first two submodules in upper and lower arms. Scale: (a) (d) (e) (f) x-axis: 0.01 s/div. (b) (c) x-axis: 10 s/div.

surface, but most of the time, the vertical distance between the submarine and the water surface will be greater than 30 meters to enhance its concealment. In reality, the submarine generator-motor system is usually composed of multiple machines. For this study case, the processes of the submarine with single generator-motor set, and submerging from water surface into seabed are emulated.

1) SUBMARINE DRIVE MOTOR

Fig. 14 shows that the change of propeller speed w_m , single-phase stator current i_{sa} , load torque T_m , and electromagnetic torque T_e of submarine propulsion system from starting to stabilization. Assuming that at $t = 0$ s, the submarine completes

a certain task near the surface, or is found by radar or enemy ship in shallow water, and needs to dive in a short period of time. In this case, as shown in Fig. 14(a), the propulsion system starts and the reactor powers it at $t = 0$ s. After about 0.3 s, w_m increases rapidly and reaches a stable speed $w_m = 120$ rad/s at about 2 s, then remains unchanged. The trend of i_{sa} indicates that the motor is operating nominally. Fig. 14(b) illustrates the trend of T_m and T_e , where the load torque is calculated by (13), which is proportional to the square of w_m .

2) NUCLEAR GENERATION

Fig. 15 gives the system-level performances for nuclear reactor generator and five-level MMC converter. In this study case,

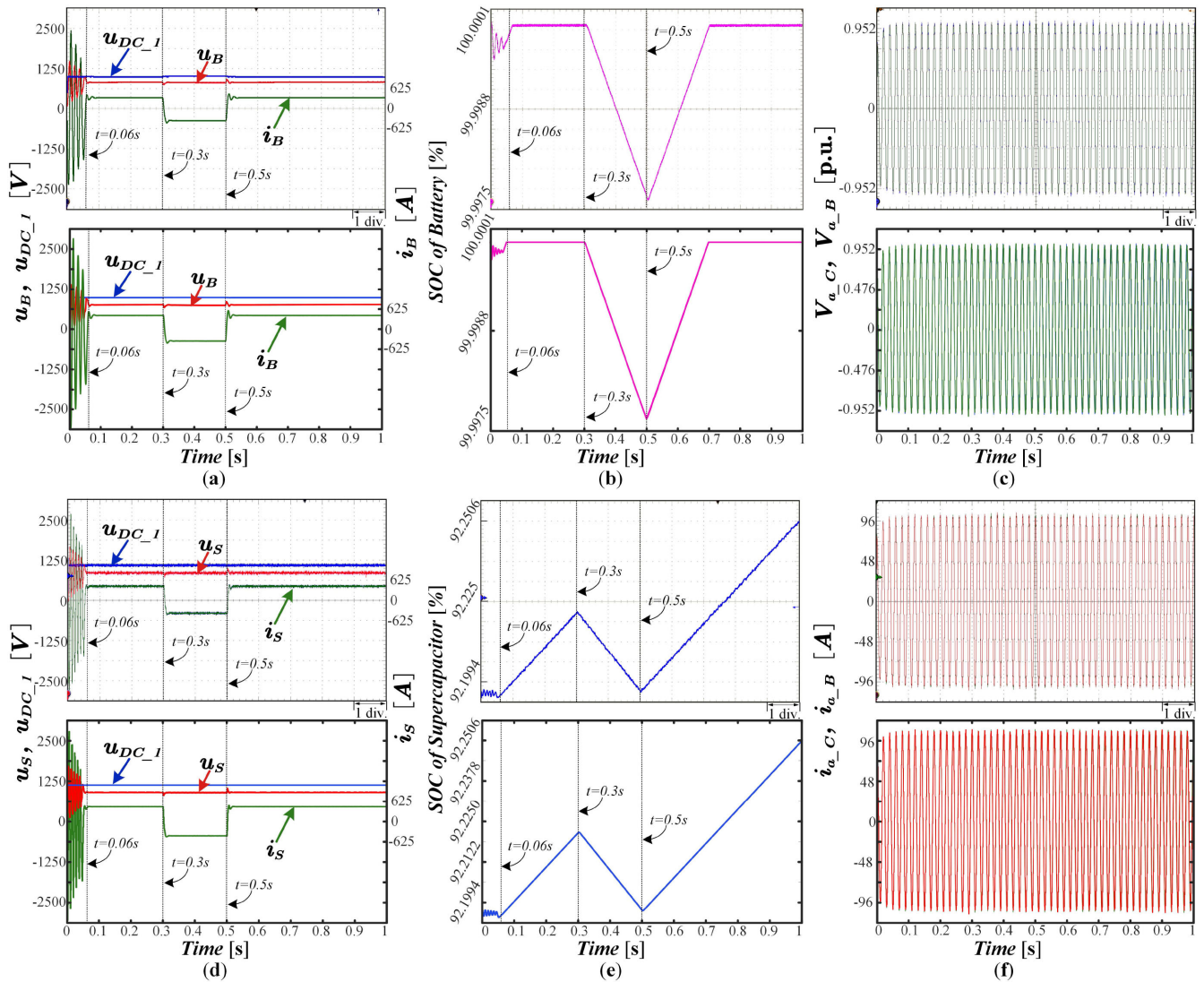


FIGURE 16. System-level results for battery and supercapacitor bank energy storage system from real-time emulation (top) and Matlab/Simulink simulation (bottom). (a) 1 kV DC bus voltage u_{DC_1} , output voltage u_B of battery bank's DAB and discharge current i_B of battery bank. (b) State-of-charge for battery bank. (c) Single-phase load voltage under battery power supply $V_{a,B}$, single phase load current under supercapacitor power supply $V_{a,C}$. (d) Output voltage u_S of supercapacitor bank's DAB and discharge current i_S of supercapacitor bank. (e) State-of-charge for supercapacitor bank. (f) Single-phase load current under battery power supply $i_{a,B}$, single phase load voltage under supercapacitor power supply $i_{a,C}$. Scale: (a) (b) (c) (d) (e) (f) x-axis: 0.1s/div.

it is assumed that the initial state of the nuclear reactor is set to the rated operating state. At $t = 0$ s, the submarine starts to submerge and generation begins to power the propulsion system. Fig. 15(a) shows the 60 Hz single phase output current and voltage of synchronous generator in per-unit value whose the nominal power and voltage are 20 MW and 13.8 kV, respectively. At about $t = 87.9$ s, when the submarine runs at a constant speed, the AC bus current is about 0.3 p.u., which provides about 5% more than the nominal power of propulsion system. The auto-stability and large inertia features of nuclear reactor lead to the slow change of reactor transients [30], [32]. Fig. 15(b) and (c) illustrate that the internal value of nuclear reactor is stabilized at the time $t = 100$ s. With the decrease of

output power P_t of steam turbine, the input signal of governor is negative, then the governor regulates the tubing valve Δy to drop, which leads to a decrease in the main steam flow. While the steam pressure ΔP_S increases slowly in the secondary loop. These changes cause the cold-leg temperature ΔT_{CL} to rise and then lead the average coolant temperature to rise. In the primary loop, negative reactivity is caused by the rise of cold-leg temperature and the movement of power control rods. After which, the neutron flux Δn , the core heat production, and the fuel temperature ΔT_F decrease, while the hot-leg temperature rises slightly. Eventually, the positive reactivity, which is caused by ΔT_F drop, offsets the previous negative reactivity, and the system becomes stable.

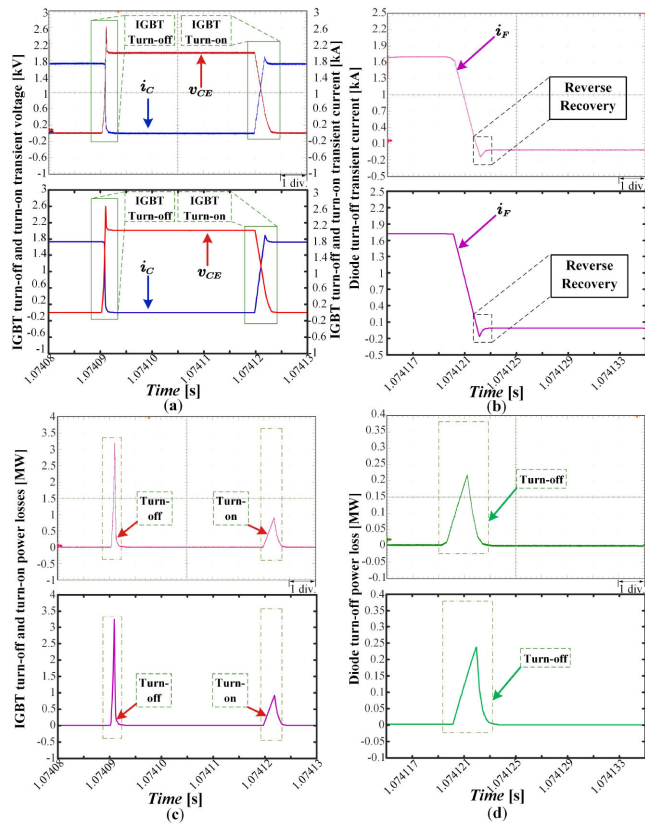


FIGURE 17. Device-level system from real-time emulation (top) and SaberRD simulation (bottom). (a) Turn-off and turn-on transient current for IGBT. (b) Turn-off transient current for diode. (c) IGBT power loss. (d) Diode power loss. Scale: (a) (c) x-axis: $5\ \mu\text{s}/\text{div}$. (b) (d) x-axis: $2\ \mu\text{s}/\text{div}$.

3) MMC-BASED PROPULSION SYSTEM

The functionality of the five-level MMC converter is tested with 20 kV DC bus voltage. Fig. 15(d) shows the line-to-line output voltage of MMC converter, which is close to 9 kV, and high symmetry can also be observed. Fig. 15(e) gives the upper arm current i_u and lower arm current i_d of MMC. Fig. 15(f) illustrates the DC voltage ripples of the first two submodules in upper arm V_{C1} , V_{C2} and lower arm V_{C5} , V_{C6} , which fluctuate at around 5 kV, indicating that the controller works properly.

B. TESTS OF ENERGY STORAGE SYSTEM

In this section, the energy storage system is divided into two parts. The first is the battery and supercapacitor energy storage system designed to the power propulsion system and the second is flywheel energy storage system used for power the submarine service load in case of emergency, shown in Fig. 16 through Fig. 19.

1) BATTERY AND SUPERCAPACITOR BANK

In this work, battery and supercapacitor banks are designed and tested separately as standby power supply for submarine service load, shown as Fig. 16. As can be seen from the figure, before $t = 0.06$ s, submarine service load is supplied

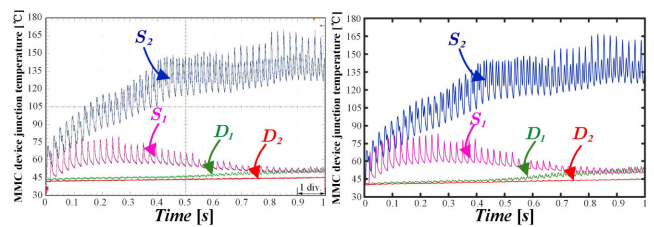


FIGURE 18. Thermal performance of device-level system from real-time emulation (left) and SaberRD simulation (right).

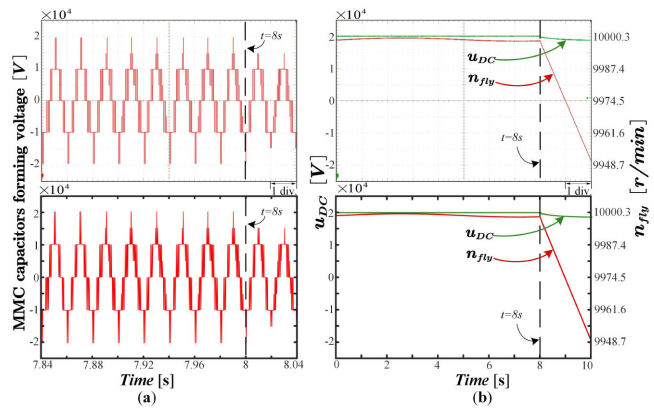


FIGURE 19. System-level results for flywheel energy storage system from real-time emulation (top) and Matlab/Simulink simulation (bottom). (a) MMC capacitor forming voltage. (b) Flywheel speed n_{fly} , and DC bus voltage u_{DC} . Scale: (a) (c) x-axis: $0.02\ \mu\text{s}/\text{div}$. (b) x-axis: $1\ \text{s}/\text{div}$.

by the DC bus, and the controllers of battery or supercapacitor banks are not activated. After that, the controller starts to work and the battery or supercapacitor bank is charged. At $t = 0.3$ s, DC bus is powered off and replaced by the battery or supercapacitor bank. When $t = 0.5$ s, DC bus power supply is restored, then the battery or supercapacitor bank changes to the charging state. Fig. 16(a) and (d) illustrate that 1 kV DC bus voltage $u_{DC,1}$, output voltage and current of battery and supercapacitor bank, respectively. The fluctuation of DC bus voltage and battery or supercapacitor bank output voltage at 0.3 s and 0.5 s is almost negligible. Both output voltage and current of battery or supercapacitor bank is set to 800V and 400A. Fig. 16(b) and (c) give that the change of SOC of battery and supercapacitor bank in which the initial state is set to 100% and 92%, respectively. Under ideal conditions, the submarine service load can be powered by battery or supercapacitor bank for about 2 hours or 15 minutes. Fig. 16(c) and (f) shows that the single-phase voltage and current of submarine service load with different power supply conditions, respectively, which indicates that both the battery and supercapacitor bank are working normally.

In terms of MMC device-level test results, a five-level MMC inverter, indicated in Fig. 12, is employed to perform the device-level emulation results in Fig. 17 by utilizing the data-sheet curve fitting model [48]–[52]. Both IGBT turn-on and turn-off's transient current and voltage curves can be observed in Fig. 17(a). Reverse recovery phenomena occurs

TABLE 2. Impedances for Thermal Network

Thermal impedance	Z_{thjc}				Z_{thch}	Z_{thha}
	$i = 1$	$i = 2$	$i = 3$	$i = 4$	$i = 5$	$i = 6$
$R_{th}^{i,IGBT} [K/kW]$	1.601	1.765	0.358	0.328	1	10
$\tau_{th}^{i,IGBT} [s]$	0.581	0.059	0.006	0.001	3	45
$R_{th}^{i,Diode} [K/kW]$	1.606	1.759	0.357	0.323	1	10
$\tau_{th}^{i,Diode} [s]$	0.584	0.059	0.006	0.001	3	45

when the diode turns-off in Fig. 17 (b). Fig. 17(c) and (d) illustrate the power losses of IGBT and diode, respectively. As seen in Fig. 18, the junction temperature of S_1 and S_2 are much higher than their corresponding anti-parallel diode D_2 and D_1 under the same switching frequency because of the higher switching energy loss in IGBT, shown in Fig. 17(c) and (d). S_1 overheat occurs at the beginning of thermal stress testing for higher switching frequency and current rating, which indicates the importance of complex nuclear powered submarine emulation for the evaluation of the renovated power electronic system. The thermal impedances of the devices [40], are shown in Table 2.

2) FLYWHEEL

In this work, the flywheel energy storage system is used to power the submarine propulsion system under certain conditions. According to the (16) and (17), it can be deduced that energy stored E is proportional to the moment of inertia J and square of the instantaneous speed w , where J is designed to be $1000 \text{ kg} \cdot \text{m}^2$ and the rated speed of flywheel is set to 10000 rpm (1047 rad/s), so the useful amount of energy stored is about 411MJ per flywheel. In this test, two flywheels are switched to power the submarine propulsion system at $t = 8 \text{ s}$. It can be seen from the Fig. 19(a) and (b), at $t = 8 \text{ s}$, the MMC converter forming voltage and DC bus voltage start to fall slowly. In Fig. 19(b), the speed of the single flywheel has decreased by about 5.7 rad/s, resulting about 5.95 MJ energy loss. In this case, ten pairs of flywheels could power the submarine propulsion system for about 22 minutes.

V. CONCLUSION AND FUTURE WORK

This paper proposed an MVDC-based real-time nuclear submarine power distribution system emulation on a multi-FPGA hardware platform, which is validated by Matlab/Simulink at system-level ($20 \mu\text{s}$ per time-step) and SaberRD at device-level (400 ns per time-step). The entire system performance including generation, MMC-based motor propulsion system, energy storage system, and the submarine service load was analyzed and discussed in detail. In the future work, a multi-domain simulation with detailed component modeling, such as considering the effect of the roll and rhythm of the sea to the reactor and thermal control, and its real-time implementation will be carried out to help engineers further their exploration of optimization and design of complex systems on the submarine [53].

APPENDIX A PARAMETERS OF MVDC NUCLEAR SUBMARINE POWER DISTRIBUTION SYSTEM

See Table 3.

TABLE 3. Parameters of MVDC Power Subsystems on Nuclear Submarine

Nuclear generation system	
Nominal voltage of main DC bus	20kV
Reactor thermal power	110MW
Reactor effective power	27500hp
Synchronous generator nominal power	20MW
Synchronous generator nominal voltage (l-l)	13.8kV
Synchronous generator nominal frequency	60Hz
Submarine propulsion motor	
Nominal power	5.7MW
Nominal voltage	9kV
Rated frequency	60Hz
Stator, rotor resistance	0.0256Ω, 0.0213Ω
Stator and rotor inductance	0.75mH
Energy storage system	
Input, output voltage of DAB module	1kV, 800V
Filter capacitance	0.005F
Filter inductance	0.2μH
Battery bank	
Rated capacity	920Ah
Fully charged voltage	800V
Cut-off Voltage	515.4V
Nominal discharge current	400A
Supercapacitor bank	
Rated voltage	802V
Rated capacitance	500F
Equivalent DC series resistance	0.0021Ω
Flywheel	
Stator phase resistance	2.875Ω
d-axis, q-axis inductance	8.5mH, 8.5mH
Magnet flux linkage	8.5mH
Flux linkage	0.258Wb
Inertia	1000kg · m ²
Submarine service load (non-critical)	
Input, output voltage of DC/DC converter	1kV, 800V
Filter capacitance	5000μF
Filter inductance	400μH
Input, output voltage of DC/AC converter	800V, 380V
Filter capacitance	5000μF
Filter inductance	1.5mH
Active power of RLC load	50kW
Submarine service load	
Input, output voltage of isolated DC/DC converter	20kV, 8kV
Filter capacitance	5mF
Filter inductance	0.1mH
IGBT of ABB® 5SNA 2000K450300	
IGBT collector-emitter voltage	4500V
IGBT DC collector current	2000A
IGBT input, output capacitance	211nF, 15nF
IGBT reverse transfer capacitance	4.2nF
IGBT internal gate resistor	0.16Ω

REFERENCES

- [1] A. S. McLaren, "Analysis of the under-ice topography in the arctic basin as recorded by the USS nautilus during August 1958," *Arctic*, pp. 117–126, 1988.

- [2] An analysis of the navys fiscal year 2020 shipbuilding plan. Oct. 2019. [Online]. Available: <https://news.usni.org/2019/10/09/cbo-analysis-of-u-s-navy-fy-2020-shipbuilding-plan>
- [3] D. Bosich, A. Vicenzutti, R. Pelaschiar, R. Menis, and G. Sulligoi, "Toward the future: The MVDC large ship research program," in *Proc. AEIT Int. Annu. Conf.*, Naples, 2015, pp. 1–6.
- [4] I. Chung *et al.*, "Integration of a bi-directional DC-DC converter model into a large-scale system simulation of a shipboard MVDC power system," in *Proc. IEEE Electric Ship Technol. Symp.*, Baltimore, MD, 2009, pp. 318–325.
- [5] "IEEE recommended practice for 1 kV to 35 kV medium-voltage DC power systems on ships," *IEEE Std. 1709-2018*, pp. 1–54, Dec. 2018.
- [6] E. Skjong, R. Volden, E. Rdskar, M. Molinas, T. A. Johansen, and J. Cunningham, "Past, present, and future challenges of the marine vessels electrical power system," *IEEE Trans. Transport. Electric.*, vol. 2, no. 4, pp. 522–537, Dec. 2016.
- [7] Z. Jin, G. Sulligoi, R. Cuzner, L. Meng, J. C. Vasquez, and J. M. Guerrero, "Next-generation shipboard DC power system: Introduction smart grid and DC microgrid technologies into maritime electrical networks," *IEEE Electric. Mag.*, vol. 4, no. 2, pp. 45–57, Jun. 2016.
- [8] G. Yang, F. Xiao, X. Fan, R. Wang, and J. Liu, "Three-phase three-level phase-shifted PWM DCDC converter for electric ship MVDC application," *IEEE J. Emerg. Sel. Topics Power Electron.*, vol. 5, no. 1, pp. 162–170, Mar. 2017.
- [9] N. Doerry, J. Amy, and C. Krolick, "History and the status of electric ship propulsion, integrated power systems, and future trends in the U.S. navy," *Proc. IEEE*, vol. 103, no. 12, pp. 2243–2251, Dec. 2015.
- [10] W. Ren *et al.*, "Interfacing issues in real-time digital simulators," *IEEE Trans. Power Del.*, vol. 26, no. 2, pp. 1221–1230, Apr. 2011.
- [11] Z. Huang and V. Dinavahi, "An efficient hierarchical zonal method for large-scale circuit simulation and its real-time application on more electric aircraft microgrid," *IEEE Trans. Ind. Electron.*, vol. 66, no. 7, pp. 5778–5786, Jul. 2019.
- [12] S. Cao, N. Lin, and V. Dinavahi, "Mitigation of subsynchronous interaction in hybrid AC/DC grid with renewable energy using faster-than-real-time dynamic simulation," early access, *IEEE Trans. Power Syst.*, pp. 1–10, 2020.
- [13] T. Duan and V. Dinavahi, "Adaptive time-stepping universal line and machine models for real time and faster-than-real-time hardware emulation," *IEEE Trans. Ind. Electron.*, vol. 67, no. 8, pp. 6173–6182, Aug. 2020.
- [14] A. Myaang and V. Dinavahi, "FPGA-based real-time emulation of power electronic systems with detailed representation of device characteristics," *IEEE Trans. Ind. Electron.*, vol. 58, no. 1, pp. 358–368, Jan. 2011.
- [15] G. G. Parma and V. Dinavahi, "Real-time digital hardware simulation of power electronics and drives," *IEEE Trans. Power Del.*, vol. 22, no. 2, pp. 1235–1246, Apr. 2007.
- [16] T. Liang and V. Dinavahi, "Real-time system-on-chip emulation of electrothermal models for power electronic devices via hammerstein configuration," *IEEE J. Emerg. Sel. Topics Power Electron.*, vol. 6, no. 1, pp. 203–218, Mar. 2018.
- [17] G. Yang, F. Xiao, X. Fan, R. Wang and J. Liu, "Three-phase three-level phase-shifted PWM DCDC converter for electric ship MVDC application," *IEEE J. Emerg. Sel. Topics Power Electron.*, vol. 5, no. 1, pp. 162–170, Mar. 2017.
- [18] T. Karla, J. Tarnawski, and K. Duzinkiewicz, "Hardware-software implementation of basic principles simulator of nuclear reactor processes," *Acta Energetica*, vol. 2, no. 27, pp. 107–112, Apr. 2016.
- [19] M. Andrus *et al.*, "Real-time simulation-based design of a power-hardware-in-the-loop setup to support studies of shipboard MVDC issues," in *Proc. IEEE Electric Ship Technol. Symp.*, Baltimore, MD, 2009, pp. 142–151.
- [20] M. Bosworth, D. Soto, M. Sloderbeck, J. Hauer and M. Steurer, "MW-scale power hardware-in-the-loop experiments of rapid power transfers in MVDC naval shipboard power," in *Proc. Electric Ship Technol. Symp.*, VA, 2015, pp. 459–463.
- [21] J. Siegers and E. Santi, "Stability analysis and control design for an all-electric ship MVDC power distribution system using a passivity based stability criterion and power hardware-in-the-loop simulation," in *Proc. IEEE Electric Ship Technol. Symp.*, Alexandria, VA, 2015, pp. 86–92.
- [22] The United States naval nuclear propulsion program. (Nov. 2015). [Online]. Available: https://www.energy.gov/sites/prod/files/2017/08/f36/nuclear_propulsion_program_8--30-2016percent5B1percent5D.pdf
- [23] S. Rippon, "History of the PWR and its worldwide development," *Energy Policy*, vol. 12, no. 3, pp. 259–265, 1984.
- [24] Nuclear-powered ships. (Jul. 2020). [Online]. Available: <https://www.world-nuclear.org/information-library/non-power-nuclear-applications/transport/nuclear-powered-ships.aspx>
- [25] T. W. Kerlin and E. M. Katz, "Pressurized-water-reactor modeling for long-term power-system-dynamics simulations," *Final Rep. (No. EPRI-EL-3087-VOL. 2)*, Tennessee Univ., 1983.
- [26] T. Ichikawa and T. Inoue, "Light water reactor plant modeling for power system dynamics simulation," *IEEE Trans. Power Syst.*, vol. 3, no. 2, pp. 463–471, May. 1988.
- [27] M. S. Di Lascio, R. Moret, and M. Poloujadoff, "Reduction of program size for long-term power system simulation with pressurized water reactor," *IEEE Power Eng. Rev.*, vol. PER-3, no. 3, pp. 43–43, Mar. 1983.
- [28] B. Puchalski, T. A. Rutkowski, and K. Duzinkiewicz, "Nodal models of pressurized water reactor core for control purposesa comparison study," *Nucl. Eng. Des.*, vol. 322, pp. 444–463, 2017.
- [29] M. S. D. Lascio, R. Moret, and M. Poloujadoff, "Reduction of program size for long-term power system simulation with pressurized water reactor," *IEEE Trans. Power App. Syst.*, vol. PER-3, no. 3, pp. 43–43, Mar. 1983.
- [30] J. J. Duderstadt and L. J. Hamilton, *Nuclear Reactor Analysis*. New York, NY, USA: Wiley, pp. 233–556, 1976.
- [31] T. Ichikawa and T. Inoue, "Light water reactor plant modeling for power system dynamics simulation," *IEEE Trans. Power Syst.*, vol. 3, no. 2, pp. 463–471, May. 1988.
- [32] J. H. Rust, *Nuclear Power Safety*, Oxford, UK: Pergamon, pp. 181–193, 1997.
- [33] "IEEE guide for synchronous generator modeling practices and applications in power system stability analyses," *IEEE Std. 1110-2002 (Revision IEEE Std. 1110-1991)*, pp. 1–80, Nov. 2003.
- [34] M. Hagiwara and H. Akagi, "Control and experiment of pulsewidth-modulated modular multilevel converters," *IEEE Trans. Power Electron.*, vol. 24, no. 7, pp. 1737–1746, Jul. 2009.
- [35] F. Blaschke, "The principle of field orientation as applied to the new transvector closed-loop system for rotating-field machines," *Siemens Rev.*, vol. 34, no. 3, pp. 217–220, 1972.
- [36] P. Karamanakos, P. Stolze, R. M. Kennel, S. Manias, and H. D. T. Mouton, "Variable switching point predictive torque control of induction machines," *IEEE J. Emerg. Sel. Topics Power Electron.*, vol. 2, no. 2, pp. 285–295, Jun. 2014.
- [37] M. A. Fnaiech *et al.*, "A measurement-based approach for speed control of induction machines," *IEEE J. Emerg. Sel. Topics Power Electron.*, vol. 2, no. 2, pp. 308–318, Jun. 2014.
- [38] Z. Shen and V. Dinavahi, "Real-time MPSoC-based electrothermal transient simulation of fault tolerant MMC topology," *IEEE Trans. Power Deliv.*, vol. 34, no. 1, pp. 260–270, Feb. 2019.
- [39] N. Lin and V. Dinavahi, "Dynamic electro-magnetic-thermal modeling of MMC-based DCDC converter for real-time simulation of MTDC grid," *IEEE Trans. Power Deliv.*, vol. 33, no. 3, pp. 1337–1347, Jun. 2018.
- [40] Z. Shen and V. Dinavahi, "Real-Time device-Level transient electrothermal model for modular multilevel converter on FPGA," *IEEE Trans. Power Electron.*, vol. 31, no. 9, pp. 6155–6168, Sep. 2016.
- [41] T. Liang and V. Dinavahi, "Real-time device-level simulation of MMC-based MVDC traction power system on MPSoC," *IEEE Trans. Transport. Electric.*, vol. 4, no. 2, pp. 626–641, Jun. 2018.
- [42] P. C. Krause, O. Wasynczuk, and S. D. Sudhoff, *Analysis of Electric Machinery*, Piscataway, NJ, USA: IEEE Press, 2002.
- [43] N. Chase and P. M. Carrica, "Submarine propeller computations and application to self-propulsion of DARPA suboff," *Ocean Eng.*, vol. 60, pp. 68–80, 2013.
- [44] O. Tremblay and L. A. Dessaint, "Experimental validation of a battery dynamic model for EV applications," *World Electr. Veh. J.*, vol. 3, no. 2, pp. 289–298, 2009.
- [45] H. Miniguano, A. Barrado, C. Fernandez, P. Zumel, and A. Lzaro, "A general parameter identification procedure used for the comparative study of supercapacitors models," *Energies*, vol. 12, no. 9, pp. 1776, 2019.
- [46] R. Ayyanar, R. Giri, and N. Mohan, "Active input-voltage and load-current sharing in input-series and output-parallel connected modular DC-DC converters using dynamic input-voltage reference scheme," *IEEE Trans. Power Electron.*, vol. 19, no. 6, pp. 1462–1473, Nov. 2004.

- [47] ABB 5SNA 2000K450300 stackpak IGBT module datasheet [Online]. Available: <https://library.e.abb.com/public/8d0f218db8df4641a4bf7c978dd2d239/5SNApercent202000K450300percent205SYApercent201431-02percent2001-2018.pdf>
- [48] N. Lin and V. Dinavahi, "Behavioral device-Level modeling of modular multilevel converters in real time for variable-speed drive applications," *IEEE J. Emerg. Sel. Topics Power Electron.*, vol. 5, no. 3, pp. 1177–1191, Sep. 2017.
- [49] N. Lin, B. Shi and V. Dinavahi, "Non-linear behavioural modelling of device-level transients for complex power electronic converter circuit hardware realisation on FPGA," *IET Power Electron.*, vol. 11, no. 9, pp. 1566–1574, Aug. 2018.
- [50] N. Lin and V. Dinavahi, "Detailed device-Level electrothermal modeling of the proactive hybrid HVDC breaker for real-time hardware-in-the-Loop simulation of DC grids," *IEEE Trans. Power Electron.*, vol. 33, no. 2, pp. 1118–1134, Feb. 2018.
- [51] W. Wang, Z. Shen and V. Dinavahi, "Physics-based device-level power electronic circuit hardware emulation on FPGA," *IEEE Trans. Ind. Inform.*, vol. 10, no. 4, pp. 2166–2179, Nov. 2014.
- [52] H. Bai, C. Liu, A. K. Rathore, D. Paire and F. Gao, "An FPGA-based IGBT behavioral model with high transient resolution for real-time simulation of power electronic circuits," *IEEE Trans. Ind. Electron.*, vol. 66, no. 8, pp. 6581–6591, Aug. 2019.
- [53] T. I. B. A. R. Dahl *et al.*, "Marine vessel and power plant system simulator," *IEEE Access*, vol. 3, pp. 2065–2079, Oct. 2015.



WEIRAN CHEN (Student Member, IEEE) received the B.Eng. degree in electrical engineering from Harbin Engineering University, Harbin, Heilongjiang, China, in 2018. He is currently working toward the M.Sc. degree in electrical and computer engineering with the University of Alberta, Edmonton, AB, Canada. His research interests include real-time simulation of power systems, power electronic systems, and field programmable gate arrays.



TIAN LIANG (Member, IEEE) received the B.Eng. degree in electrical engineering from Nanjing Normal University, Nanjing, Jiangsu, China, in 2011, the M.Eng. degree from Tsinghua University, Beijing, China, in 2014, the Ph.D. degree in energy systems from the University of Alberta, Edmonton, AB, Canada, in 2020. His research interests include real time simulation of power systems, power electronics, artificial intelligence, field programmable gate arrays, and system on chip.



VENKATA DINAVAH (Fellow, IEEE) received the B.Eng. degree in electrical engineering from the Visveswaraya National Institute of Technology (VNIT), Nagpur, India, in 1993, the M.Tech. degree in electrical engineering from the Indian Institute of Technology (IIT) Kanpur, India, in 1996, and the Ph.D. degree in electrical and computer engineering from the University of Toronto, Ontario, Canada, in 2000. Currently, he is a Professor with the Department of Electrical and Computer Engineering, University of Alberta, Edmonton, AB, Canada. His research interests include real-time simulation of power systems and power electronic systems, electromagnetic transients, device-level modeling, large-scale systems, and parallel and distributed computing.